Research article

Impact of varied zeolite materials on nickel catalysts in CO$_2$ methanation

Penghui Yan [a], Hong Peng [a,*], Xuankun Wu [a], Hesamoddin Rabiee [a,b], Yilun Weng [c],
Muxina Konarova [a], John Vogrin [d], Alexandra Rozhkovskaya [d], Zhonghua Zhu [a,*]

[a] School of Chemical Engineering, The University of Queensland, St Lucia, QLD 4072, Australia
[b] Centre for Future Materials, University of Southern Queensland, Springfield, QLD 4300, Australia
[c] Australian Institue for Bioengineering and Nanotechnology, The University of Queensland, St Lucia, 9 QLD, 4072, Australia
[d] Zeotech Limited, Brisbane Technology Park, QLD, Eight Mile Plains, 4113, Australia

A B S T R A C T

Ni catalysts supported on 4A, 5A, 13X, ZSM-5, and BEA zeolites were prepared using the vacuum-heating method for CO$_2$ methanation. These support materials play a pivotal role in shaping the catalysts' properties and their catalytic performance. High-resolution high-angle annular dark-field scanning transmission electron microscopy (HAADF-STEM) and energy-dispersive X-ray spectroscopy (EDS) mappings suggest a significant concentration of Ni nanoparticles situated on the external surfaces of catalysts with low Si/Al ratios zeolites (Ni-4A, Ni-5A, and Ni-13X). These Ni nanoparticles exhibit characteristics of weaker metal-support interaction, lower metal reduction temperatures, and moderate H$_2$ adsorption activity. Moreover, these low Si/Al ratio zeolites demonstrate robust CO$_2$ adsorption activity. These properties endow Ni-5A and Ni-13X catalysts with heightened CO$_2$ conversion (70.4–70.9%) and methane selectivity (92.4–96.4%). In contrast, high Si/Al ratio zeolite-based catalysts (Ni-ZSM-5 and Ni-BEA) exhibit smaller Ni particles, strong metal-support interaction and weaker CO$_2$ adsorption activity, resulting in reduced CO$_2$ methanation activity and decreased methane selectivity (71.2–73.4%). The normalized CO$_2$ conversion rate presents a correlation with the average Ni particle size.

1. Introduction

The escalating levels of CO$_2$ emissions in the atmosphere, driven by rapid economic growth, have placed an immense strain on our environment, resulting in critical issues such as global warming, ocean acidification, and climate change [1]. To counteract these environmental challenges, there has been a growing acknowledgment of the potential to convert CO$_2$ into high-value chemicals [2–4]. This strategy not only aids in reducing carbon emissions but also aligns with the principles of sustainable development. While considerable attention has been directed towards photo- and electro-driven CO$_2$ conversion methods [5,6], it's essential to underscore that thermal-conversion of CO$_2$ remains the most efficient and robust approach. Exploring innovative pathways for directly converting CO$_2$ into specific target products holds paramount importance [7–10]. CO$_2$ methanation, specifically the reaction of CO$_2$ with H$_2$ to produce methane (CH$_4$) through the Sabatier reaction, emerges as a promising method for large-scale energy storage. Synthetic natural gas, formed through this process, serves as a suitable energy carrier with long-term storage ability and compatible with existing infrastructure [11]. It holds the potential to provide a renewable, carbon–neutral source of CH$_4$, thereby stabilizing energy supply, contingent on efficient CO$_2$ capture from biomass-derived gas sources

and the atmosphere [12]. The Sabatier reaction, as described by CO$_2$ + 4H$_2$ ↔ CH$_4$ + 2H$_2$O; ΔH$_0$r (298 K) = − 165 kJ/mol (1), is intrinsically constrained by equilibrium [13]. Recognizing this limitation, researchers have increasingly explored sorption-enhanced CO$_2$ methanation, a process that removes water from the reaction mixture, thereby surpassing equilibrium yields, in accordance with Le Chatelier's principle [14].

Ni-based catalysts have garnered substantial attention for CO$_2$ methanation due to their commendable catalytic performance and cost-effectiveness [15–18]. Nevertheless, the presence of CO as a by-product can lead to the formation of Ni carbonyl species and carbon deposition on the Ni surface, resulting in catalytic instability or deactivation [19–21]. The performance of catalysts in CO$_2$ methanation is intricately linked to factors such as metal dispersion, support, alkalinity, and metal-support interaction [21–25]. The properties of support material play a crucial role in influencing these interactions. The Ni/CeO$_2$ catalyst has been used for CO$_2$ methanation due to the oxygen vacancies of CeO$_2$, which promote the adsorption and activation of CO$_2$ [26,27]. The Ni/CeO$_2$-(111) catalyst, characterized by a robust metal-support interaction, demonstrates improved reaction activity and CH$_4$ selectivity [28]. Moreover, it is reported the Y$_2$O$_3$, ZrO$_2$, La$_2$O$_2$CO$_3$, and perovskites supported Ni catalysts exhibit a commendable stability in CO$_2$

---

* Corresponding authors.
  E-mail addresses: h.peng2@uq.edu.au (H. Peng), z.zhu@uq.edu.au (Z. Zhu).

methanation [29–33].

Zeolites (such as 4A, 5A, 13X, ZSM-5, BEA, MCM-41, SBA-15), renowned for their specific microporous structure and high surface area, have emerged as promising supports for the development of metal catalysts [19,34–40]. It is reported CO_2 methanation is promoted by the hydrophobic zeolites with higher Si/Al ratio [41]. LTA-4A and LTA-5A, which exhibit CO_2 adsorption capacity of 1.25 and 3.28 mol/kg, respectively [42,43], facilitate the formation of metal nanoparticles, enhancing CO_2 methanation activity [21,35,36]. Wei [13] investigated the influence of nickel precursors on the 5A and 13X catalysts and proposed that the Ni-13X catalyst with nickel citrate being precursor improved the metal dispersion, resulting in a 79 % CO_2 conversion with 100 % selectivity towards CH_4. Keavan [44] reported that Ni nanoparticles (~19 nm) over Yttria Stabilized Zirconia (YSZ) prepared by wet impregnation with $Ni(EDTA)^{2-}$ exhibited a higher CH_4 selectivity compared to that prepared by nickel nitrate and mechanical mixing with NiO nanopowder (<50 nm), presumably due to its moderate Ni particle size. Wang [45] proposed that the small Ni nanoparticles (3.5 nm) with increased defect sites facilitate the formation of initial monodentate carbonate, which are active sites in CO_2 methanation reaction. In contrast, the larger nickel particles (7.5 nm) promote the formation of CO. The influence of the framework of zeolites on CO_2 methanation was investigated by Bacariza [46]. The Ni/USY showed the best performance compared to Ni/BEA, Ni/ZSM-5, and Ni/MOR due to its weakest interaction with water. The Ni/BEA with an increased Ni dispersion exhibited a higher CO_2 conversion and CH_4 selectivity compared to Ni/HZSM-5 and Ni-MOR.

While zeolite-supported nickel catalysts have been utilized in CO_2 methanation reactions, the impact of diverse supports (including the low Si/Al ratio 4A, 5A, 13X and high Si/Al ratios ZSM-5 and BEA zeolites) on nickel crystallite size, surface properties, metal-support interactions, and their consequent effects on catalytic activity in CO_2 methanation under the same conditions have not been thoroughly investigated. Therefore, the primary objective of this study is to conduct a comprehensive performance comparison of low Si/Al ratio zeolites (4A, 5A, 13X) and high Si/Al ratio zeolites (HZSM-5, HBEA) supported similar Ni loading (5 wt%) catalysts in CO_2 methanation reactions. The study elucidates how the zeolite structure influences Ni particle size, consequently influencing CO_2 methanation activity. Higher concentrations of mesopore surface area in HZSM-5 and BEA zeolites promote the formation of smaller Ni particles, fostering strong interaction with the support and limiting CO_2 methanation activity. In contrast, 5A and 13X zeolites, characterized by a restricted number of mesopores, facilitate the production of bulk Ni species on the external surface, enhancing CO_2 methanation activity. Furthermore, the research identifies an optimal average Ni particle size for CO_2 methanation at approximately 8.8 nm, showcasing the highest CO_2 conversion rate. Additionally, this study observes that the introduction of moisture results in a slightly higher catalyst deactivation rate compared to the dry feedstock.

2. Experimental section

2.1. Catalyst preparation

Support materials, namely 4A, 5A, and 13X zeolites purchased from Sigma, HBEA and HZSM-5 zeolites from Zeolyst International, were utilized in the study. Zeolite-supported nickel catalysts were prepared using a recently developed vacuum-heating technique [47]. In applying the vacuum-heating method, a predetermined mass of nickel nitrate hexahydrate ($Ni(NO_3)_2 \cdot 6H_2O$) supplied by Sigma-Aldrich was dissolved in distilled water and then impregnated onto pre-calcined 4A, 5A, 13X, HZSM-5, and HBEA zeolites. The wet solids were dried at 100 °C for 6 h, followed by vacuum-heating at 450 °C for 2 h. The vacuum-heated samples were coded as Ni-4A, Ni-5A, Ni-13X, Ni-ZSM-5, Ni-BEA. The samples were reduced at 500 °C for 2 h under H_2 flow (50 mL/min) for characterization and catalytic tests.

2.2. Catalyst characterization

The X-ray powder diffraction (XRD) patterns were acquired in the range of 2θ = 5-90° using a Bruker D8 advance diffractometer with Cu Kα radiation. The contents of Ni were analysed by ICP-OES and the Si/Al ratios of catalysts were determined by X-ray fluorescence (XRF). The X-ray photoelectron spectroscopy (XPS) spectra were obtained from a Kratos Axis Ultra XPS with a 165 mm hemispherical electron energy analyzer and a monochromatic Al Kα (1486.6 eV) radiation source at 15 kV (10 mA). XPS data was analysed by CASA® software (calibrated to the C 1 s signal at 284.8 eV).

Transmission electron microscopy (TEM) imaging was carried out in a field emission transmission electron microscope (HF5000), equipped with an energy-dispersive X-ray spectroscopy (EDS). Samples were prepared using an ethanol dispersion method and placed on a copper grid. The metal dispersion was calculated based on the average particle size obtained from TEM [48,49].

Nitrogen adsorption–desorption isotherms were investigated at −196 °C in a Micromeritics TriStar II surface area analyser to determine the surface area and pore properties of samples. Prior to nitrogen adsorption, the sample was heated in vacuum at 200 °C for 8 h using a Micromeritics VacPrep 061 sample preparation device. The volume and surface area of micro- and *meso*-pore, as well as the pore diameter were determined by the t-plot and Barrett-Joyner-Halenda (BJH) models.

Temperature-programmed desorption (TPD) of NH_3 was measured using BELCAT-B. The samples underwent reduction with pure H_2 (50 mL/min) at 500 °C for 2 h before adsorption. Subsequently, they were exposed to a flow of ammonia (20 mL/min) at 150 °C for 20 min, and thermal conductivity detector (TCD) signals were recorded from 50 to 600 °C under a flow of He gas (20 mL/min). H_2-TPD and CO_2-TPD experiments, closely mirroring NH_3-TPD procedures, were conducted in BELCAT-B, with the exception that H_2 and CO_2 were adsorbed at 50 °C. Temperature-programmed reduction (TPR) was also performed via BELCAT-B to determine the reducibility of catalyst. The catalyst was first activated in He (20 mL/min) at 500 °C for 30 min to remove water and other impurities, followed by cooling to 50 °C. Reduction was carried out using a H_2 flow (30 mL/min) from 50 °C to 850 °C with a heating rate of 10 °C/min. The hydrogen consumption was recorded by TCD.

2.3. Catalyst test

The catalytic tests were carried out in a continuous flow reactor under atmospheric pressure.

Before the catalytic tests, samples were pre-reduced at 500 °C for 2 h. The reduction peak was absent in the H_2-TPR profile of pre-reduced Ni-BEA-vac sample (Fig. S1), suggesting NiO undergoes complete reduction to metallic Ni^0 under the reduction conditions of 500 °C for 2 h, in line with our previous studies [50]. Reactivity tests were accomplished using a feed constituted by H_2 and CO_2 at a molar ratio of 4:1 and a total flow of 100 mL min⁻¹, with the flows controlled by a Brooks mass flow controller. A common practice in CO_2 methanation studies involves utilizing a feed gas with H_2/CO_2 ratio of 4 and excluding N_2, as extensively documented in the literature [51,52]. The mass of catalyst and gas hourly space velocity (GHSV) used in all the catalytic tests was kept constant (30 000 mL $h^{-1} \cdot g_{cat}^{-1}$). The reaction was performed at temperatures ranging from 300 to 400 °C. The concentrations of CO, CH_4, and CO_2 were analyzed using an online 2014 Shimadzu Gas Chromatograph (GC), equipped with a ShinCarbon column (2 m, argon as carrier gas), TCD and flame ionization detector (FID). BELMass spectrometry was also used online to determine the time-on-stream intensity of CH_4 (m/z = 16), CO (m/z = 28), and CO_2 (m/z = 44). CO and CH_4 were the sole products identified in the process of CO_2 hydrogenation.

The CO_2 conversion, CO and CH_4 selectivity were defined as below:

$$X_{CO2} = \frac{n_{CO2in} - n_{CO2out}}{n_{CO2in}} \times 100\%$$

$$S_{CO} = \frac{n_{COout}}{n_{CO2in} - n_{CO2out}} \times 100\%$$

$$S_{CH4} = \frac{n_{CH4out}}{n_{CO2in} - n_{CO2out}} \times 100\%$$

3. Results and discussion

3.1. The structure characterization of catalysts

The Nitrogen adsorption–desorption isotherms of catalysts are shown in Fig. 1a, while the surface area and pore volume calculated via *t*-plot and BJH methods are listed in Table 1. It can be seen from Table 1 and Fig. 1a, the micropores were almost absent in the Ni-4A catalyst, which could be ascribed to the small pore size of 4A zeolite, restricting the entrance of N$_2$ (0.36 nm). Ni-5A and Ni-13X exhibited a significant reduced value of micropore surface area compared to parent 5A and 13X, suggesting the micropores were partially blocked by the Ni bulk

nanoparticles. The Ni-ZSM-5 shows a lower micropore surface area compared to Ni-5A and Ni-13X, however, it exhibits a higher mesopores surface area (69 cm^3/g), which could be attributed to its intersecting and three-dimensional channel system [53]. The Ni-BEA catalyst displays a high micropore surface area as well as mesopore surface, suggesting a bimodal pore distribution, in line with the type I-IV isotherms and H4 hysteresis loops observed in Fig. 1a. It has been reported the zeolites with bimodal pore distribution promote the metal dispersion [54]. The pore sizes of 4A and 5A and 13X are approximately 0.4 nm, 0.5 nm and 1 nm, respectively. ZSM-5 and BEA show pore diameters of 0.54 × 0.56 nm and 0.64 × 0.76 nm, respectively [55,56]. Given that the kinetic diameters of CO$_2$, CH$_4$, and CO are 0.33 nm, 0.38 nm, and 0.38 nm, respectively [57], it can be inferred that the entrance and diffusion of feedstock and products will not undergo significant hindrance over 13X and BEA-based catalysts. In contrast, the smaller pores of 4A may restrict the diffusion of feedstock and products.

XRD patterns of the reduced catalysts are presented in Fig. 1b. The diffraction peaks of zeolites are distinctly visible, signifying that the
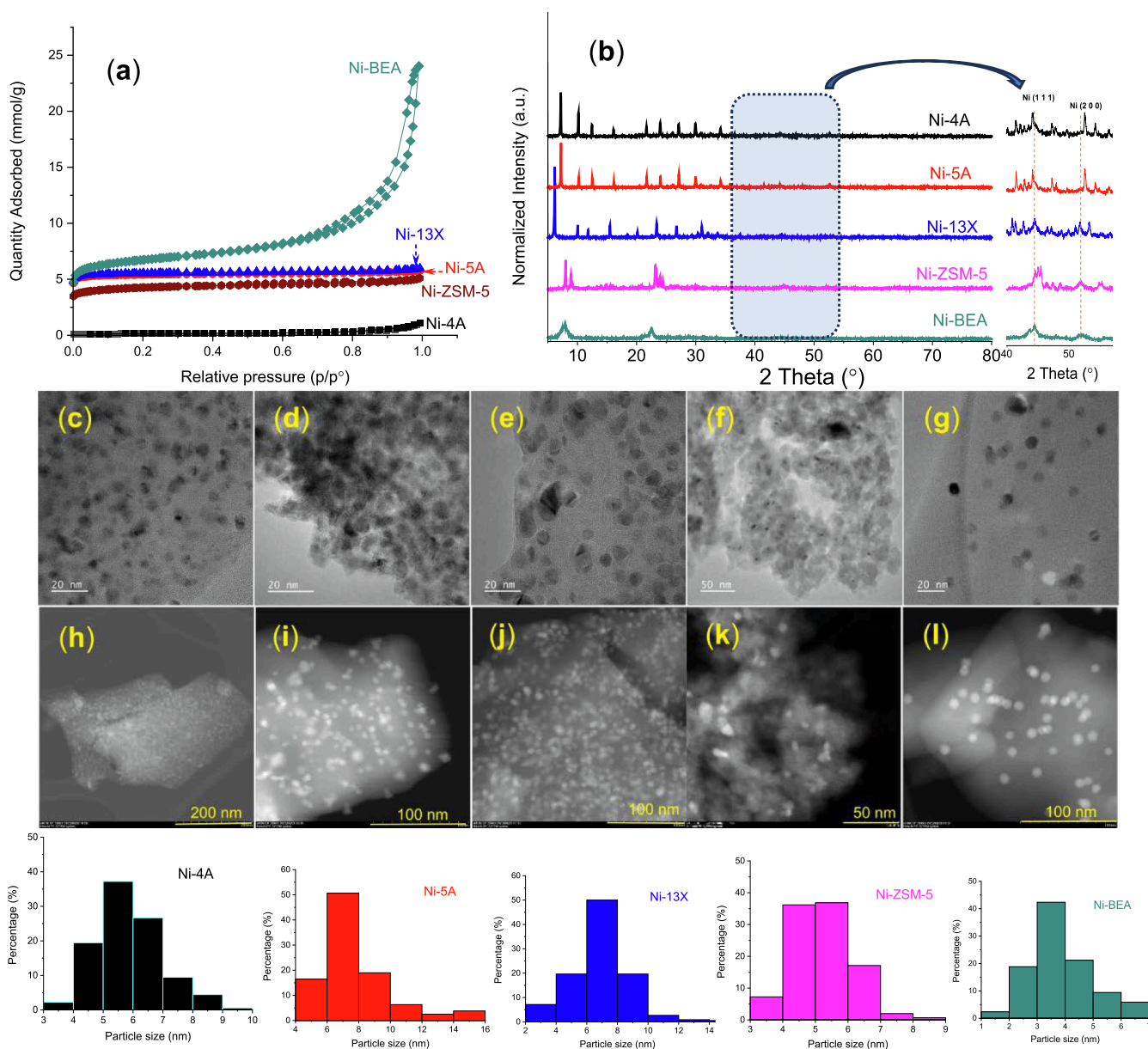

Fig. 1. (**a**) Nitrogen adsorption–desorption isotherms of reduced catalysts. (**b**) XRD patterns of reduced samples; HAADF-STEM images of reduced (**c, h**) Ni-4A, (**d, i**) Ni-5A, (**e, j**) Ni-13X, (**f, k**) Ni-BEA, and (**g, l**) Ni-ZSM-5 catalysts.

Table 1
Textural and physicochemical characteristics of supports and reduced catalysts.

Sample	Ni content[a] (wt%)	Si/Al atomic ratio[b]	$S_{micro}^{[c]}$ (m²/g)	$S_{meso}^{[d]}$ (m²/g)	$V_{micro}^{[c]}$ (cm³/g)	$V_{meso}^{[d]}$ (cm³/g)	d_{Ni} (nm) [e]
4A	–	1	1	1	0	0	–
5A	–	1	451	21	0.23	0.02	–
13X	–	1.25	567	36	0.29	0.03	–
ZSM-5	–	11.7	260	44	0.13	0.04	–
BEA	–	11.8	322	250	0.16	0.32	–
Ni-4A	4.1	1	3	9	0	0.02	5.9
Ni-5A	4.4	1	343	24	0.17	0.02	7.6
Ni-13X	5.3	1.25	349	27	0.18	0.02	6.8
Ni-ZSM-5	4.2	11.7	224	69	0.11	0.05	5.2
Ni-BEA	4.3	11.8	310	206	0.16	0.31	3.8

[a] The Ni contents of catalysts were obtained from ICP-OES analysis.
[b] The Si/Al ratios were measured by XRF analysis.
[c] From N₂ adsorption measurements (*t*-plot). S-$_{micro}$ = micropore surface area. V-$_{micro}$ = micropore volume.
[d] From N₂ adsorption measurement (BJH method, 1.7–300 nm), S-$_{meso}$ = mesopore surface area. V-$_{meso}$ = mesopore volume.
[e] d_{Ni} = average Ni particle size (based on TEM analysis).

addition of a small quantity of Ni to the supports does not disturb the crystal structures of the zeolites. In contrast, the diffraction peaks associated with Ni are nearly absent, a phenomenon that may be attributed to either the low metal content or the finely dispersed Ni species falling below the detection limits of the XRD technique. However, upon scaling up the patterns in the range of 40–55 °, the diffraction peaks of Ni (1 1 1) and Ni (2 0 0) were discerned in Ni-13X, Ni-ZSM-5, and Ni-BEA. Notably, Ni-BEA exhibits a larger Full Width at Half Maximum (FWHM) (1.3°) at 51.8 °, followed by Ni-ZSM-5 (0.8°) and Ni-13X (0.4°). This observation suggests the formation of smaller Ni particles in Ni-BEA.

HAADF-STEM was employed to further investigate the Ni species distribution. As shown in Fig. 1(c–e, h–j) a significant higher concentration of Ni nanoparticles is observed on the external surface of zeolites 4A, 5A, and 13X. This observation suggests that the small pores in Ni-4A, Ni-5A, and Ni-13X catalysts limit the entry of metal species, resulting in a heightened concentration of nanoparticles formed outside the pores. In contrast, the concentration of Ni nanoparticles on the external surface of Ni-ZSM-5 and Ni-BEA was significantly reduced compared to Ni-4A, Ni-5A, and Ni-13X, which could be attributed to the pore structures of ZSM-5 and BEA. The three-dimensional 10-membered and 12-membered rings of ZSM-5 and BEA could facilitate the dispersion of Ni species. Although TEM analysis revealed the presence of bulk Ni particles in Ni-4A and Ni-5A, the corresponding Ni diffraction peaks were not evident in Fig. 1b. One plausible explanation for this discrepancy could be attributed to their low Si/Al ratio (1) and the interaction with high extra-framework Al, Na, and Ca ions. The presence of these ions on the external surface might lead to the adsorption of Ni species, resulting in the agglomeration of Ni particles and the formation of bulk Ni species interacting with surface Al, Na and Ca, thereby hindering the detection of Ni diffractions.

The agglomeration of Ni species on the external surface of 4A, 5A, and 13X was further confirmed through EDS mappings. As shown in Fig. 2(a–c), distinct bulk cyan-colored Ni nanoparticles were clearly detected on the Ni-4A, Ni-5A, and Ni-13X catalysts. While the Ni nanoparticles were also observed on Ni-ZSM-5 and Ni-BEA, they appeared smaller in size. Moreover, the density of nanoparticles on the external surface of ZSM-5 and BEA was significantly reduced compared to Ni-4A, Ni-5A, and Ni-13X, suggesting that a substantial portion of Ni particles were of smaller size, distributed both on the external and internal pore surface.

The reducibility of NiO species over the prepared catalysts was investigated by H₂ temperature-programmed reduction, with the results shown in Fig. 3a. There are two main reduction peaks over the developed catalysts. The low-temperature peak range from 350 to 480 °C could be attributed to the bulk NiO nanoparticles that possess a weak interaction with supports and present in the zeolite external surface [58,59]. The high-temperature reduction peak from 480 to 700 °C could be attributed to the smaller NiO particles possessing a strong metal-support interaction [60,61]. A significant amount of NiO species over Ni-13X and Ni-4A catalysts was reduced at lower temperature (300–450 °C), presumably due to a higher concentration of bigger Ni nanoparticles located in the external surface. While Ni-5A also exhibits a high concentration of larger Ni nanoparticles on the external surface, it demonstrates a higher reduction temperature centered around (440 °C) compared to Ni-13X and Ni-4A. This phenomenon can be attributed to the interaction of Ni with the Ca species in 5A, thereby delaying the reduction of Ni species. Conversely, the Ni-BEA catalyst showed a significant amount of Ni species reduced at 544 °C, indicating a strong metal-support interaction. Combining STEM and XRD analysis, it becomes evident that Ni-BEA featured a narrow distribution of small Ni particles, suggesting that these small Ni particles readily formed a robust interaction with the support. Furthermore, Table S1 summarizes the peak area of the reduction peak. The reduction observed above 500 °C can be attributed to the presence of Ni clusters and single atoms [47], which possess the capability to penetrate the pores. As depicted, Ni-5A (26.6 %) and Ni-13X (13.7 %) exhibited a lower amount of high-temperature (high-T) reduction sites, suggesting a limited number of Ni sites can access the pores. In contrast, Ni-BEA displayed a higher high-T reduction peak area (47.3 %), indicating a significant proportion of Ni sites can penetrate the pores.

XPS profiles provided further insights into elemental and chemical state information of Ni species. The catalysts were offline reduced at 500 °C for 2 h. As displayed in Fig. 3b, two main peaks, centered at 853.2 eV and 855.8 eV, were observed in the cases of Ni-4A, Ni-5A, and Ni-13X, corresponding to Ni $2p_{3/2}$ of NiO and Ni(OH)$_x$, respectively [62,63]. Conversely, only the Ni(OH)$_x$ peak was detected in Ni-ZSM-5 and Ni-BEA catalysts. This observation aligns with previous studies, which suggest that Ni(OH)$_x$ species are formed as a result of the surface layer of NiO interacting with moisture in the air [64,65]. Thus, the absence of NiO species in Ni-ZSM-5 and Ni-BEA suggests a higher concentration of surface Ni species and improved metal dispersion compared to Ni-4A, Ni-5A, and Ni-13X, in line with TEM analysis.

Ni-BEA catalyst exhibited the highest desorption of H₂, followed by Ni-ZSM-5, Ni-4A, Ni-13X, and Ni-5A, as illustrated in the H₂-TPD profiles (Fig. 4a). This order aligns with the particle size distribution. Ni-BEA, characterized by enhanced metal dispersion and smaller Ni particle size, facilitates the H₂ adsorption/desorption. In contrast, bulk Ni particles with limited metal surface exhibit a reduced quantity of desorbed H₂. Notably, Ni-BEA displayed a significantly higher H₂ desorption temperature (506 °C) compared to Ni-ZSM-5, Ni-4A, Ni-5A, and Ni-13X, suggesting a robust interaction between H species and small metal. The CO₂-TPD profiles of the reduced catalysts, as shown in Fig. 4b, reveal that Ni-5A, Ni-4A, and Ni-13X display significantly higher
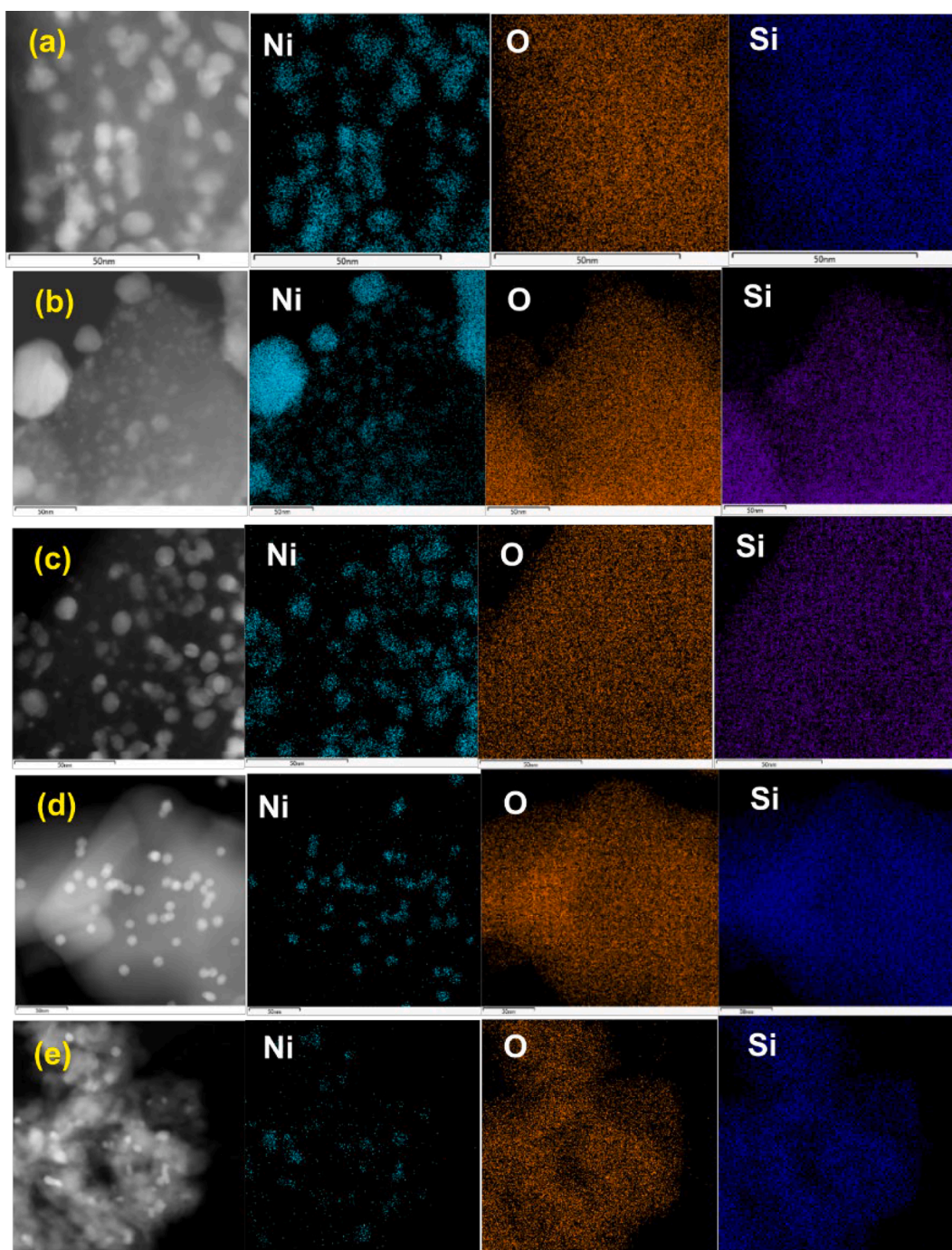
Fig. 2. EDS-mappings of reduced (**a**) Ni-4A, (**b**) Ni-5A, (**c**) Ni-13X, (**d**) Ni-ZSM-5, and (**e**) Ni-BEA.

desorbed CO_2 in comparison to Ni-ZSM-5 and Ni-BEA. This discrepancy can be attributed to the low Si/Al ratios in 4A, 5A, 13X zeolites (Table 1), which means more polar (hydrophilic) surface thus possessed a strong affinity to CO_2 [66–68]. Furthermore, when comparing 13X with Ni-13X catalyst (Fig. S2), it is evident that the introduction of metal species results in a decreased CO_2 adsorption activity. The acid properties of reduced catalysts were investigated via NH_3-TPD, with results shown in Fig. S3. All catalysts demonstrated a notable concentration of acid sites, with particular emphasis on Ni-5A and Ni-13X. These two catalysts exhibited significantly higher concentration of low-temperature acid sites, attributed to their elevated levels of Lewis acidic extra-framework Al species.

3.2. Catalytic performance on CO_2 methanation

The CO_2 methanation tests were conducted within a continuous flow reactor, and the corresponding results are depicted in Fig. 5. All catalysts exhibited an upsurge in CO_2 conversion as the reaction temperature increased, implying that higher temperatures facilitated CO_2 activation (Fig. 5a). Significantly, Ni-4A, Ni-5A, and Ni-13X outperformed Ni-BEA and Ni-ZSM-5 in terms of CO_2 conversion, indicative of the lower CO_2 activity associated with catalysts featuring high Si/Al ratios and small Ni particles. The performance results of the support (13X) in CO_2 methanation are illustrated in Fig. S4. The figure reveals no CO_2 conversion, suggesting that the support has no discernible impact on the CO_2 methanation process.
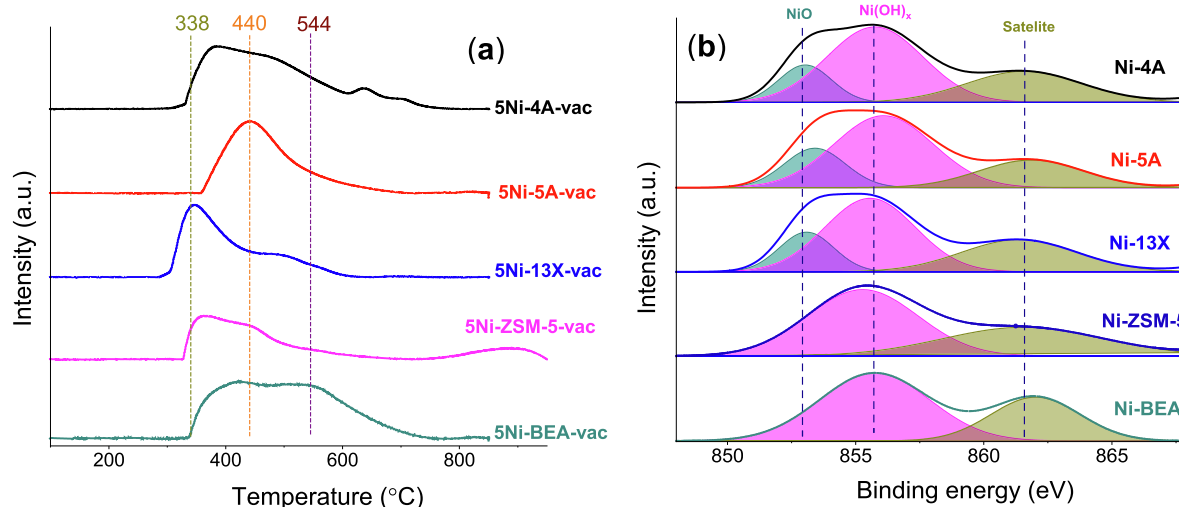
Fig. 3. (**a**) H$_2$-TPR profiles of samples and (**b**) Ni 2p$_{3/2}$ spectra of reduced samples.
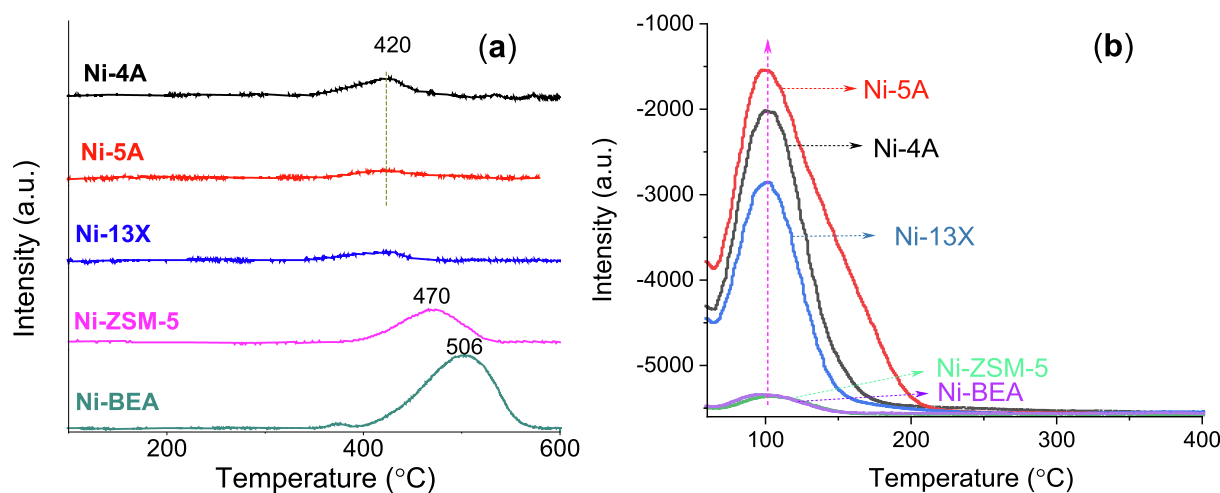

Fig. 4. (**a**) H$_2$-TPD and (**b**) CO$_2$-TPD profiles of reduced catalysts. The intensity was normalized by sample mass.

With the escalation of temperature, CH$_4$ selectivity consistently increased, while CO selectivity diminished for all catalysts as indicated by Fig. 5b–c. This behavior signified that higher temperature favoured CH$_4$ selectivity, whereas lower temperatures promoted the formation of CO. Ni-5A, Ni-13X and Ni-4A, exhibited significantly higher methane yield compared to Ni-ZSM-5 and Ni-BEA catalysts at 350 and 400 °C. This suggests that smaller Ni species present in Ni-ZSM-5 and Ni-BEA catalysts have lower methanation activity.

To provide further insight, *in situ* mass spectrometry was employed to analyze the time-on-stream intensity of CO$_2$, CO and CH$_4$ in the products (as shown in Fig. 5d–f). As shown in Fig. 5d, CO$_2$ concentration exhibited a declining trend with increasing temperature, aligning with GC-FID analysis. The concentration of methane exhibits a substantial increase for Ni-13X, Ni-4A, and Ni-5A as the reaction temperature rose from 350 to 400 °C (Fig. 5e). In contrast, Ni-ZSM-5 and Ni-BEA showed a slight increase in CH$_4$ intensity with increasing reaction temperature. The concentration of CO increased as the reaction temperature rose from 300 to 350 °C across all catalysts. However, for Ni-13X, Ni-4A, and Ni-5A catalysts, the CO concentration decreased as the reaction temperature was further increased from 350 °C to 400 °C. In contrast, the CO intensity continued to rise with increasing temperature up to 400 °C for Ni-ZSM-5 and Ni-BEA catalysts. These results underscore that the

presence of small Ni species (3.8–5.2 nm) over Ni-ZSM-5 and Ni-BEA leads to lower CO$_2$ methanation activity compared to Ni-4A, Ni-5A, and Ni-13X with larger Ni nanoparticles (5.9–7.6 nm) and stronger CO$_2$ adsorption activity.

The analysis of CO/CO$_2$ ratios in the reactor effluent stream is detailed in Table 2. At a reaction temperature of 350 °C, Ni-BEA and Ni-ZSM-5 catalysts exhibit low CO/CO$_2$ ratios, indicating a tendency toward the reverse water–gas shift reaction. Conversely, Ni-13X, Ni-5A, and Ni-4A catalysts demonstrate higher CO/CO$_2$ ratios, suggesting a shift toward CO formation. Notably, Ni-13X and Ni-5A catalysts show enhanced hydrogenation of CO to methane, reflected in their higher methane selectivity. At 400 °C, there's a significant increase in the CO/CO$_2$ ratios, aligning with the known endothermic nature of the reverse water–gas shift reaction favored at elevated temperatures. However, our results reveal variations among the catalysts. Despite higher CO/CO$_2$ ratios, Ni-BEA and Ni-ZSM-5 show limited effectiveness in converting CO to methane, possibly due to their lower hydrogenation capacity. In contrast, Ni-5A exhibits both a low CO/CO$_2$ ratio and high methane selectivity, indicating a robust capability for hydrogenation and promoting CO methanation.

Equilibrium compositions were assessed using the R$_{Equil}$ model in Aspen Plus at 300 °C, 350 °C, and 400 °C (Tables S2–S5). The
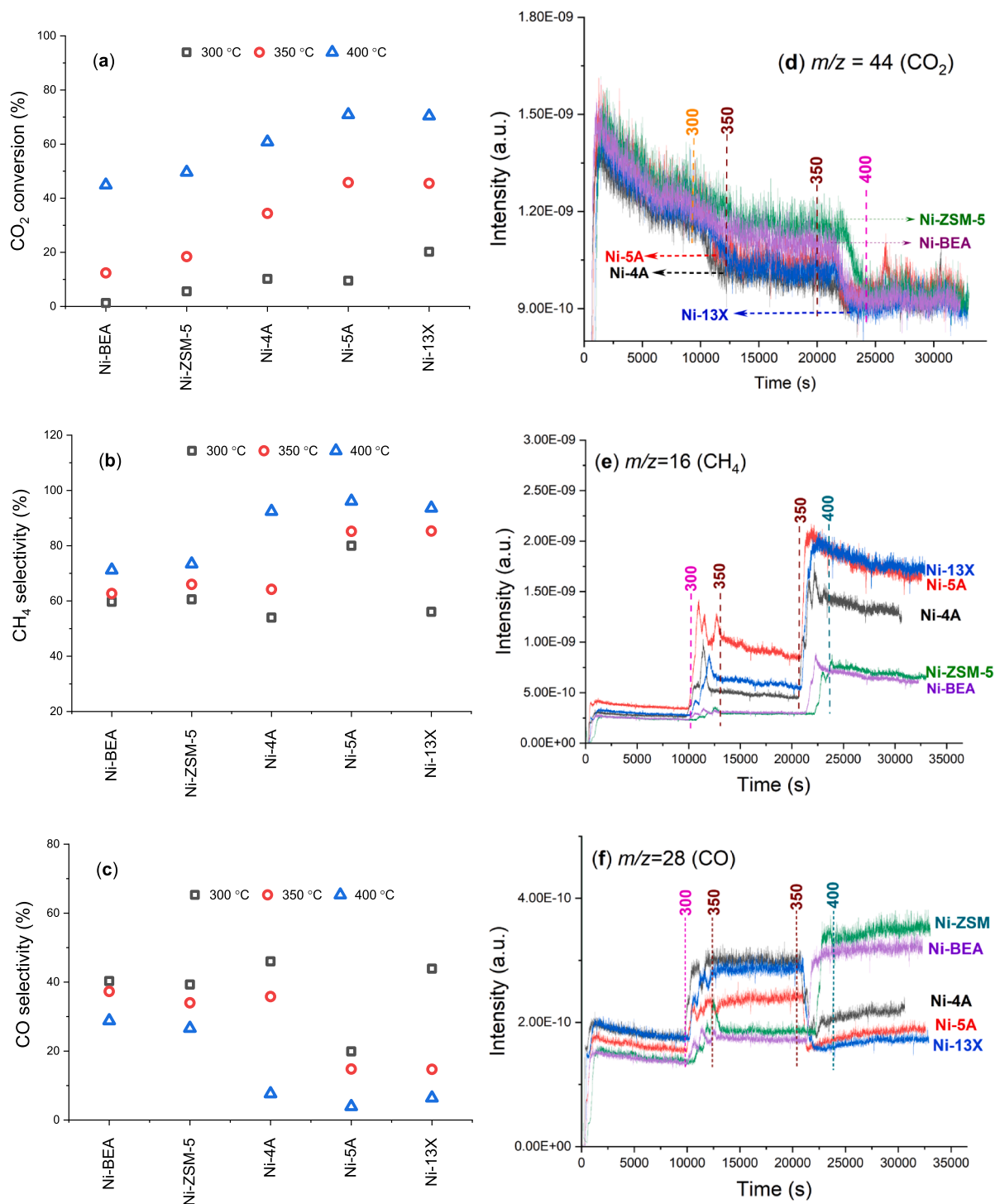
Fig. 5. (a) CO_2 conversion and (b) CH_4 selectivity and (c) CO selectivity. The intensity of (d) CO_2, (e) CH_4 and (f) CO as measured by *in situ* mass spectrometry. Reaction conditions: H_2: 80 mL/min, CO_2: 20 mL/min, catalyst mass: 0.2 g, reaction temperature: 300 °C, 350 °C and 400 °C with each temperature held for 3 h.

experimental CO/CO_2 ratios consistently surpassed those predicted by the R_{Equil} model, suggesting that the water–gas shift reaction did not reach equilibrium under the experimental conditions.

Based on XPS, H_2-TPD, and H_2-TPR analyses, it is evident that the smaller Ni species in Ni-BEA demonstrate a robust metal-support interaction, resulting in an increased electron transfer from metal species to the support. Furthermore, it is worth noting that the high Si/Al zeolite catalysts, namely ZSM-5 and BEA, exhibit significantly lower CO_2 adsorption activity in comparison to the catalysts with low Si/Al zeolites

(4A, 5A, and 13X). The diminished hydrogenation activity observed in conjunction with the low CO_2 adsorption activity over Ni-ZSM-5 and Ni-BEA catalysts contributes to their reduced CO_2 methanation activity. However, it is noteworthy that the primary factor appears to be the low hydrogenation activity of the small metal species. The relationships between the normalized CO_2 conversion rate (TOF-$_{CO2}$) and CH_4 formation rate (TOF-$_{CH4}$) were illustrated in Fig. 6. Notably, Ni-5A demonstrated the highest TOF-$_{CO2}$ (67.3 min^{-1}) and TOF-$_{CH4}$ (57.4 min^{-1}), succeeded by Ni-13X (49.7 min^{-1}, 42.4 min^{-1}), Ni-4A (41.8

Table 2
CO/CO$_2$ ratio in the effluent stream at 350 °C and 400 °C.

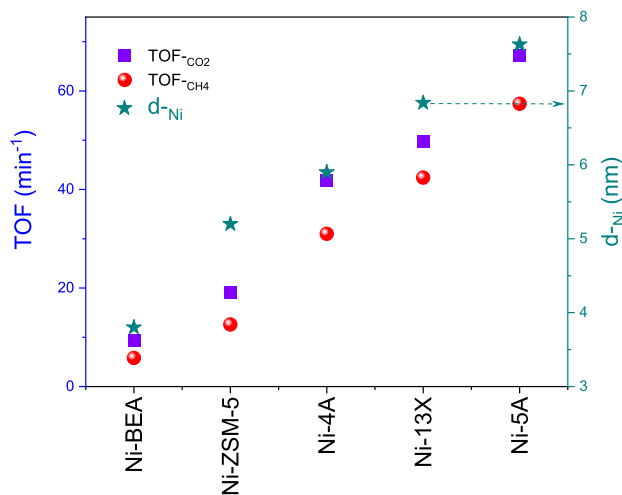| Sample	CO/CO$_2$ ratio in effluent stream	
	350 °C	400 °C
Ni-BEA	0.052799	0.235689667
Ni-ZSM-5	0.076666682	0.262711059
Ni-13X	0.122724807	0.15134875
Ni-5A	0.125062768	0.09483322
Ni-4A	0.135292716	0.11790753

Fig. 6. The relationships of normalized CO$_2$ conversion rate (TOF-$_{CO2}$) and CH$_4$ formation rate (TOF-$_{CH4}$), (the rates were based on the surface Ni-metal loading*dispersion), and Ni average particle size (d-$_{Ni}$). These relationships were established at a reaction temperature of 350 °C.

min^{-1}, 31.0 min^{-1}), Ni-ZSM-5 (19.1 min^{-1}, 12.6 min^{-1}) and Ni-BEA (9.3 min^{-1}, 5.8 min^{-1}). This observation suggests that the reaction rate is not solely dependent on the concentration of surface Ni; otherwise, all catalysts would exhibit similar TOF values.

Furthermore, the sequence of TOF values aligns with the trend in Ni average particle size (d-$_{Ni}$). This correlation indicates that the surface of bulk Ni particles possesses robust CO$_2$ methanation activity. It's worth noting that this trend is consistent with our previous findings, where we observed that the surface of bulk Ni species exhibits higher hydrogenation activity compared to that of small Ni species [47].

Beierlein [69] suggested that CO$_2$ methanation on Ni-Al$_2$O$_3$ catalysts was not a structure-insensitive reaction; instead, the conversion is linked to the metal surface area. However, our studies lead to the conclusion that small Ni particles diminish the activity of catalysts in CO$_2$ methanation. This disparity could be attributed to the substantial loadings (14–88 wt%) and particle sizes (5–91 nm) in their study. Hydrogenation activity predominantly relies on the concentration of surface Ni when dealing with Ni nanoparticles larger than 5 nm [47]. The presence of small Ni nanoparticles and nanoclusters (<4 nm), exhibiting a robust metal-support interaction, results in a weakened hydrogenation activity [47]. This characteristic facilitates the direct decomposition of intermediates (HCOO*, CO*) to CO [70,71]. In contrast, bulk nickel species, with a potent hydrogenation activity, are more likely to promote the further hydrogenation of intermediates to CH$_4$ [44,72].

The increased CO$_2$ adsorption activity observed in low Si/Al zeolites (4A, 5A, 13X) could potentially contribute to enhancing the CO$_2$ methanation activity of the catalysts. However, this may not be the rate-determining step, as evidenced by Ni-4A. Although Ni-4A exhibits higher CO$_2$ adsorption activity, its methanation activity is lower compared to Ni-13X. Furthermore, Ni-4A, Ni-5A, and Ni-13X exhibit

over 10 times higher CO$_2$ adsorption compared to Ni-ZSM-5 and Ni-BEA. However, the CO$_2$ conversion is only twice higher at 350 °C. Moreover, Ni-5A and Ni-13X, characterized by the highest concentration of metal species situated on the external surface, demonstrated elevated CO$_2$ methanation activity. BEA and ZSM-5 zeolites featuring increased mesopores facilitate metal dispersion but diminish the CO$_2$ methanation activity due to the reduced hydrogenation activity over smaller Ni species. This suggests that the zeolite structure plays a crucial role in determining the size of metal particles and the interaction between metal and support, consequently influencing CO$_2$ methanation activity. Furthermore, Ni-ZSM-5, Ni-BEA, Ni-4A, and Ni-13X exhibit a considerable concentration of acid sites, as illustrated in Fig. S3. However, despite the elevated acidity, Ni-ZSM-5 and Ni-BEA demonstrate significantly lower activity, suggesting that acid sites may play a less substantial role in CO$_2$ methanation reactions for these catalysts.

To investigate the influence of metal particle size on CO$_2$ methanation, we prepared Ni-5A-ethanol and Ni-5A-H$_2$O catalysts, using ethanol and H$_2$O as solvents (detailed catalyst preparation is provided in the SI). Ni-5A-ethanol exhibited the largest average Ni particle size (13.0 nm), followed by Ni-5A-H$_2$O (8.8 nm) and Ni-5A (7.6 nm), as indicated by XRD and TEM analysis (Fig. S5). Performance results are presented in Fig. S6 and Table S6. Ni-5A-H$_2$O exhibited the highest CO$_2$ conversion (50.0 %), followed by Ni-5A (45.8 %) and Ni-5A-ethanol (30.7 %), suggesting that the CO$_2$ methanation activity can be further improved by increasing the average nickel particle size from 7.6 nm to 8.8 nm. Ni-5A-ethanol, with the largest Ni particle size (13.0 nm), demonstrated a reduced CO$_2$ conversion. The TOF-$_{CO2}$ for Ni-5A-ethanol (86.8 min^{-1}) did not show significant improvement compared to Ni-5A-H$_2$O (84.8 min^{-1}) (Table S6), suggesting that CO$_2$ methanation activity depends on the number of surface Ni sites when the Ni particle size exceeds 8.8 nm.

3.3. Stability of the 5Ni-13X catalyst in dry and wet feed gas

Catalysts commonly experience deactivation in high-temperature heterogeneous catalytic reactions due to issues such as metal sintering and coke deposition [48,73–76]. To assess the long-term stability, a durability test was conducted on the 5Ni-13X-vac catalyst at T = 400 °C and GHSV = 24,000 mL h^{-1}·g$_{cat}^{-1}$ for 50 h, with results depicted in Fig. 7. The initial conversion initiated at 72.0 %, and remarkably, it remained nearly constant throughout the entire duration, experiencing only a slight decline of 5.6 %. Moreover, the CH$_4$ selectivity remained consistent, hovering close to 95 % throughout the test. This demonstrates the catalyst's ability to selectively convert carbon dioxide to methane in extended operating conditions. In contrast, a stability test was also conducted using a dry feed gas that passed through water in a water container. Interestingly, the introduction of moisture in the feedstock reduced the catalyst's lifespan, resulting in a higher drop in CO$_2$ conversion, reaching 11.1 % compared to the dry feed gas (5.6 %) over 50 h. This phenomenon can be attributed to the formation of CO$_2$ through the water–gas shift reaction, coupled with an acceleration in Ni sintering. This observation aligns with studies by Aziz [77] and Batista [78], who reported that the presence of water in the feedstream negatively affects CO$_2$ methanation, causing a 30 % activity decrease within 5 h. Furthermore, Ren et al. explored the impact of impurities such as N$_2$, steam and O$_2$ on CO$_2$ methanation over the Ni/ZrO$_2$ [79] and La$_{2-x}$Ce$_x$NiO$_4$ [80] catalysts. The catalytic activity of Ni/ZrO$_2$ in CO$_2$ methanation exhibited the following trend under conditions of 400 °C, 1 atm, and GHSV = 10,000 h^{-1}: O$_2$ > N$_2$ > CO$_2$ > steam. Notably, the presence of O$_2$ promoted the generation of *OH groups, thereby enhancing the conversion of intermediates to methane. Moreover, the introduction of 10 % steam results in a 9 % reduction in activity over a 100-hour time-on-stream (TOS) period at 350 °C [80]. In addition, we conducted a brief examination of the impact of K (potassium) and La (lanthanum) promoters on CO$_2$ methanation (as shown in Fig. S7). The addition of K enhanced the stability of the 5Ni/13X catalyst in CO$_2$ methanation, while the La promoter expedited the deactivation of the
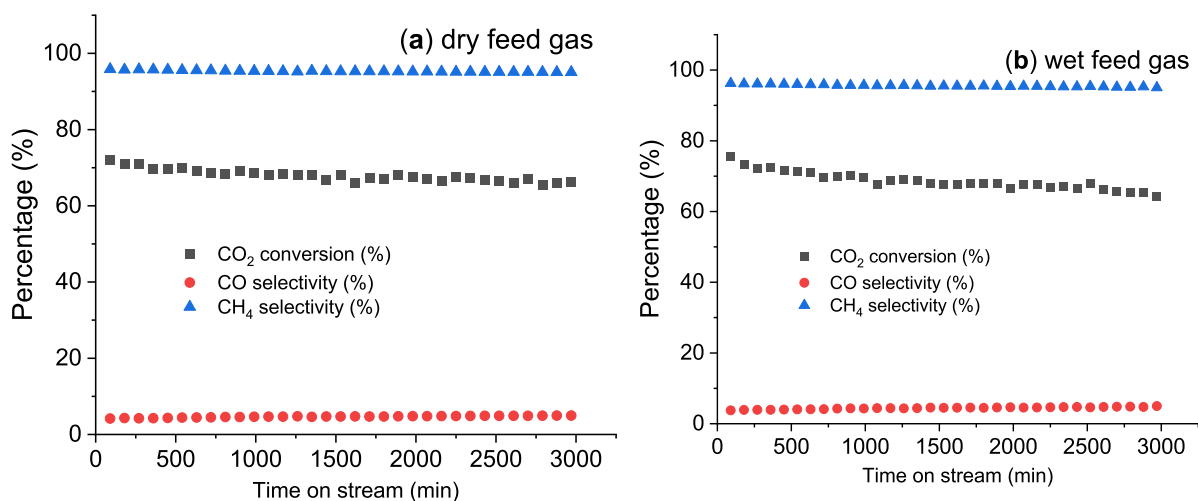
Fig. 7. CO_2 conversion and selectivity of CO and CH_4 over 5Ni-13X-vac catalyst during time of stream at 400 °C. (**a**) Dry feed gas; (**b**) wet feed gas (the feed gas passes through water). Reaction conditions: 100 mL/min of mixture gas (19 % CO_2, 4 % N_2, 77 % H_2), catalyst mass: 0.25 g.

5Ni-13X catalyst.

4. Conclusions

In summary, this investigation delved into CO_2 methanation using Ni catalysts supported by low Si/Al ratio zeolites (4A, 5A, 13X) and high Si/Al ratio zeolites (ZSM-5, BEA). High-resolution imaging techniques, including HAADF-STEM and EDS-mappings, unveiled a considerable concentration of larger Ni nanoparticles, primarily situated in the external surface region over the Ni-4A, Ni-5A and Ni-13X catalysts. These bulk Ni nanoparticles exhibited distinctive characteristics, featuring a weaker metal-support interaction, a lower reduction temperature, and medium-temperature desorption of H_2, all of which contribute to the promotion of CO_2 methanation activity. Conversely, Ni-ZSM-5 and Ni-BEA, characterized by high Si/Al ratios and extensive mesopore surface areas, displayed enhanced metal distribution and high-temperature desorption of H_2. However, they also exhibited significantly reduced CO_2 adsorption activity and decreased hydrogenation activity, resulting in diminished CO_2 conversion and CH_4 selectivity, alongside an increased selectivity toward CO. The CO_2 conversion rate rises proportionally with the augmentation of the average Ni particle size, reaching its peak at 8.8 nm.

This study underscores the significant impact of the zeolite structure in determining nickel particle size, thereby shaping the activity of CO_2 methanation. Specifically, micropore zeolites characterized by low Si/Al ratios, such as 13X and 5A, are recognized as ideal supports for methane production from CO_2. These zeolites facilitate the formation of larger Ni nanoparticles on the external surface area and enhance CO_2 adsorption, contributing to optimized performance in the process. Moreover, it was observed that the addition of K enhanced the stability of the 5Ni-13X catalyst in CO_2 methanation, while the La promoter or moisture in feedstock expedited the deactivation of the 5Ni-13X catalyst.

CRediT authorship contribution statement

Penghui Yan: Writing – original draft, Resources, Methodology, Investigation, Formal analysis, Data curation. **Hong Peng:** Writing – review & editing, Supervision, Project administration, Funding acquisition, Conceptualization. **Xuankun Wu:** Investigation, Data curation. **Hesamoddin Rabiee:** Formal analysis, Data curation. **Yilun Weng:** Formal analysis, Data curation. **Muxina Konarova:** Writing – review & editing, Resources, Data curation. **John Vogrin:** Writing – review & editing, Resources, Investigation. **Alexandra Rozhkovskaya:** Writing – review & editing, Resources, Investigation. **Zhonghua Zhu:** Writing –

review & editing, Supervision, Project administration, Funding acquisition, Conceptualization.

Declaration of competing interest

The authors declare that they have no known competing financial interests or personal relationships that could have appeared to influence the work reported in this paper.

Data availability

Data will be made available on request.

Appendix A. Supplementary data

Supplementary data to this article can be found online at https://doi.org/10.1016/j.jcat.2024.115439.

References

[1] S.J. Davis, K. Caldeira, H.D. Matthews, Future CO_2 emissions and climate change from existing energy infrastructure, Science 329 (2010) 1330–1333.
[2] P. Yan, H. Peng, J. Vogrin, H. Rabiee, Z. Zhu, Selective CO_2 hydrogenation over zeolite-based catalysts for targeted high-value products, J. Mater. Chem. A 11 (2023) 17938–17960.
[3] B. Xie, R.J. Wong, T.H. Tan, M. Higgam, E.K. Gibson, D. Decarolis, J. Callison, K. F. Aguey-Zinsou, M. Bowker, C.R.A. Catlow, J. Scott, R. Amal, Synergistic ultraviolet and visible light photo-activation enables intensified low-temperature methanol synthesis over copper/zinc oxide/alumina, Nature Commun. 11 (2020) 1615.
[4] B. Xie, T.H. Tan, K. Kalantar-Zadeh, J. Zheng, P. Kumar, J. Jiang, S. Zhou, J. Scott, R. Amal, Promoting low-temperature methanol production over mixed oxide supported cu catalysts: coupling ceria-promotion and photo-activation, Appl. Catal. b. Env. 315 (2022) 121599.
[5] H. Rabiee, J.K. Heffernan, L. Ge, X. Zhang, P. Yan, E. Marcellin, S. Hu, Z. Zhu, H. Wang, Z. Yuan, Tuning flow-through cu-based hollow fiber gas-diffusion electrode for high-efficiency carbon monoxide (CO) electroreduction to C2+ products, Appl. Catal. b: Env. 330 (2023) 122589.
[6] J. Li, L. Yuan, S. Li, Z. Tang, Y. Xu, One-dimensional copper-based heterostructures toward photo-driven reduction of CO_2 to sustainable fuels and feedstocks, J. Mater. Chem. A 7 (2019) 8676–8689.

[7] S. Kikkawa, K. Teramura, K. Kato, H. Asakura, S. Hosokawa, T. Tanaka, Formation of CH₄ at the metal-support Interface of Pt/Al₂O₃ during hydrogenation of CO₂: operando XAS-DRIFTS study, ChemCatChem 14 (2022) e202101723.

[8] H.K. Min, H. Min, S. Kweon, Y.W. Kim, S. Lee, C.H. Shin, M.B. Park, S.B. Kang, Selective hydrogenation of CO₂ to CH₄ over two-dimensional nickel silicate molecular sieves, catal, Sci. Technol. 12 (2022) 2232–2240.

[9] J. Chen, X. Wang, D. Wu, J. Zhang, Q. Ma, X. Gao, X. Lai, H. Xia, S. Fan, T. Zhao, Hydrogenation of CO2 to light olefins on cuznzr@(zn-)SAPO-34 catalysts: strategy for product distribution, Fuel 239 (2019) 44–52.

[10] J.A. Rodriguez, P. Liu, D.J. Stacchiola, S.D. Senanayake, M.G. White, J.G. Chen, Hydrogenation of CO2 to methanol: importance of metal-oxide and metal-Carbide Interfaces in the activation of CO2, ACS Catal. 5 (2015) 6696–6706.

[11] S. Ronsch, J. Schneider, S. Matthischke, M. Schluter, M. Gotz, J. Lefebvre, P. Prabhakaran, S. Bajohr, Review on methanation – from fundamentals to current projects, Fuel 166 (2016) 276–296.

[12] T. Schaaf, J. Grunig, M.R. Schuster, T. Rothenfluh, A. Orth, Methanation of CO2-storage of renewable energy in a gas distribution system, Energy Sustain. Soc. 4 (2014) 2.

[13] L. Wei, W. Haije, N. Kumar, J. Peltonen, M. Peurla, H. Grenman, W. de Jong, Influence of nickel precursors on the properties and performance of ni impregnated zeolite 5A and 13X catalysts in CO₂ methanation, Catalysis Today 362 (2021) 35–46.

[14] L.C. Buelens, V.V. Galvita, H. Poelman, C. Detavernier, G.B. Marin, Super-dry reforming of methane intensifies CO₂ utilization via le chatelier's principle, Science 354 (2016) 449–452.

[15] T.A. Le, M.S. Kim, S.H. Lee, T.W. Kim, E.D. Park, CO and CO₂ methanation over supported ni catalysts, Catal. Today 293–294 (2017) 89–96.

[16] X. Guo, A. Traitabgwong, M. Hu, C. Zuo, V. Meeyoo, Z. Peng, C. Li, Carbon dioxide methanation over nickel-based catalysts supported on Various mesoporous material, Energy Fuels 32 (2018) 3681–3689.

[17] W.L. Vrijburg, G. Garbarino, W. Chen, A. Parastaev, A. Longo, E.A. Pidko, E.J. M. Hensen, Ni-mn catalysts on silica-modified alumina for CO₂ methanation, J. Catal. 382 (2020) 358–371.

[18] A. Quindimil, U. De-La-Torre, B. Pereda-Ayo, J.A. González-Marcos, J.R. González-Velasco, Ni catalysts with la as promoter supported over Y- and BETA- zeolites for CO₂ methanation, Appl. Catal. b: Env. 238 (2018) 393–403.

[19] Y. Cui, B. Chen, L. Xu, M. Chen, C. Wu, J. Qiu, G. Cheng, N. Wang, J. Xu, X. Hu, CO₂ methanation over the ni-based catalysts supported on the hollow ZSM-5 zeolites: effects of the hollow structure and alkaline treatment, Fuel 334 (2023) 126783.

[20] A. Westermann, B. Azambre, M.C. Bacariza, I. Graca, M.F. Ribeiro, J.M. Lopes, C. Henriques, Insight into CO₂ methanation mechanism over NiUSY zeolites: an operando IR study, Appl. Catal. b: Env. 174–175 (2015) 120–125.

[21] B. Miao, S.S.K. Ma, X. Wang, H. Su, S.H. Chan, Catalysis mechanisms of CO₂ and CO methanation, catal, Sci. Technol. 6 (2016) 4048–4058.

[22] C. Italiano, J. Liorca, L. Pino, M. Ferraro, V. Antonucci, A. Vita, CO and CO₂ methanation over ni catalysts supported on CeO₂, Al₂O₃ and Y₂O₃ oxides, Appl. Catal. b: Env. 264 (2020) 118494.

[23] X. Wen, L. Xu, M. Chen, Y. Shi, C. Lv, Y. Cui, X. Wu, G. Cheng, C. Wu, Z. Miao, F. Wang, X. Hu, Exploring the influence of nickel precursors on constructing efficient ni-based CO₂ methanation catalysts assisted with in-situ technologies, Appl. Catal. b: Env. 297 (2021) 120486.

[24] J.H. Kwak, L. Kovrik, J. Szanyi, CO₂ reduction on supported Ru/Al₂O₃ catalysts: cluster size dependence of product selectivity, ACS Catal. 3 (2013) 2449–2455.

[25] L. Shen, J. Xu, M. Zhu, Y.F. Han, Essential role of the support for nickel-based CO₂ methanation catalysts, ACS Catal. 10 (2020) 14581–14591.

[26] P. Hongmanorom, J. Ashok, P. Chirawatkul, S. Kawi, Interfacial synergistic catalysis over ni nanoparticles encapsulated in mesoporous ceria for CO₂ methanation, Appl. Catal. b: Env. 297 (2021) 120454.

[27] S. Tada, H. Nagase, N. Fujiwara, R. Kikuchi, What are the best active sites for CO₂ methanation over Ni/CeO₂? Energy Fuels 35 (2021) 5241–5251.

[28] T. Pu, J. Chen, W. Tu, J. Xu, Y. Han, I.E. Wachs, M. Zhu, Dependency of CO₂ methanation on the strong metal-support interaction for supported Ni/CeO₂ catalysts, J. Catal. 413 (2022) 821–828.

[29] A. Blanco, J. Caroca, R. Tamayo, M. Flores, M. Romero-Saez, R. Espinoza-Gonzalez, F. Gracia, CO₂ methanation activity of ni-doped perovskites, Fuel 320 (2022) 123954.

[30] M. Safdar, M. González-Castaño, A. Penkova, M.A. Centeno, J.A. Odriozola, H. Arellano-García, CO₂ methanation on Ni/YMn₁₋ₓAlₓO₃ perovskite catalysts, Applied Materialstoday 29 (2022) 101577.

[31] Y. Yan, Y. Dai, Y. Yang, A.A. Lapkin, Improved stability of Y₂O₃ supported ni catalysts for CO2 methanation by precursor-determined metal-support interaction, Appl. Catal. b. Env. 237 (2018) 504–512.

[32] W. Li, X. Nie, X. Jiang, A. Zhang, F. Ding, M. Liu, Z. Liu, X. Guo, C. Song, ZrO₂ support imparts superior activity and stability of co catalysts for CO₂ methanation, Appl. Catal. b. Env. 220 (2018) 397–408.

[33] Y. Dai, M. Xu, Q. Wang, R. Huang, Y. Jin, B. Bian, C. Tumurbaatar, B. Ishtsog, T. Bold, Y. Yang, Enhanced activity and stability of Ni/La₂O₂CO₃ catalyst for CO₂ methanation by metal-carbonate interaction, Appl. Catal. b. Env. 277 (2020) 119271.

[34] Y. Cui, J. Qiu, B. Chen, L. Xu, M. Chen, C. Wu, G. Cheng, B. Yang, N. Wang, X. Hu, CO₂ methanation over Ni/ZSM-5 catalysts: the effects of support morphology and La₂O₃ modification, Fuel 324 (2022) 124679.

[35] S. Upasen, G. Sarunchot, N. Srira-ngam, Y. Poo-arporn, P. Wattanachai, P. Prasertdham, P. Ngaotrakanwiwat, J. Panpranot, S. Soisuwan, What if zeolite

[36] L. Wei, W. Haije, N. Kumar, J. Peltonen, M. Peurla, H. Grenman, W. de Jong, Can bi-functional nickel modified 13X and 5A zeolite catalysts for CO₂ methanation be improved by introducing ruthenium? Molecular Catalysis 494 (2020) 111115.

[37] W. Gac, W. Zawadzki, G. Stowik, M. Kusmiez, S. Dzwigaj, The state of BEA zeolite supported nickel catalysts in CO₂ methanation reaction, Applied Surface Science 564 (2021) 150421.

[38] L. Wei, H. Grenman, W. Haije, N. Kumar, A. Aho, K. Eranen, L. Wei, W. de Jong, Sub-nanometer ceria-promoted ni 13X zeolite catalyst for CO₂ methanation appl, Catal. a: Gen. 612 (2021) 118012.

[39] M.C. Bacariza, I. Graça, S.S. Bebiano, J.M. Lopes, C. Henriques, Micro- and mesoporous supports for CO₂ methanation catalysts: a comparison between SBA-15, MCM-41 and USY zeolite, Chem. Eng. Sci. 175 (2018) 72–83.

[40] M.C. Bacariza, I. Graça, J.M. Lopes, C. Henriques, Tuning zeolite properties towards CO₂ methanation: an overview, ChemCatChem 11 (2019) 2388–2400.

[41] M.C. Bacariza, I. Graça, J.M. Lopes, C. Henriques, Enhanced activity of CO₂ hydrogenation to CH₄ over ni based zeolites through the optimization of the Si/Al ratio, Micro. Meso. Mater. 267 (2018) 9–19.

[42] D. Saha, Z. Bao, F. Jia, S. Deng, Adsorption of CO₂, CH₄, N₂O and N₂ on MOF-5, MOF-177, and zeolite 5, Environ. Sci. Technol. 44 (2010) 1820–1826.

[43] R.V. Siriwardane, M.S. Shen, E.P. Fisher, J.A. Poston, Adsorption of CO₂ on molecular sieves and activated carbon, energy, Fuel 2 (2001) 279–284.

[44] J.K. Kesavan, I. Luisetto, S. Tuti, C. Meneghini, G. Lucci, C. Battocchio, S. Mobilio, S. Casciardi, R. Sisto, Y.S.Z. Nickel supported, The effect of ni particle size on the catalytic activity for CO₂ methanation, J. CO2 Utilization 23 (2018) 200–211.

[45] K. Wang, Y. Men, S. Liu, J. Wang, Y. Li, Y. Tang, Z. Li, W. An, X. Pan, L. Li, Decoupling the size and support/metal loadings effect of Ni/SiO₂ catalysts for CO₂ methanation, Fuel 304 (2021) 121388.

[46] M.C. Bacariza, M. Maleval, I. Graca, J.M. Lopes, C. Henriques, Power-to-methane over Ni/zeolites: influence of the framework type, Micro. Meso. Mater. 274 (2019) 102–112.

[47] P. Yan, S. Xi, H. Peng, D.R.G. Mitchell, L. Harvey, M. Drewery, E.M. Kennedy, Z. Zhu, G. Sankar, M. Stockenhuber, Facile and eco-friendly approach to produce confined metal cluster catalysts, J. Am. Chem. Soc. 145 (2023) 9718–9728.

[48] P. Yan, X. Tian, E.M. Kennedy, M. Stockenhuber, Advanced in situ IR spectroscopy study of anisole hydrodeoxygenation over Ni/SiO₂ catalysts, J. Catal. 427 (2023) 115102.

[49] A. Borodzinski, M. Bonarowska, Relation between crystallite size and dispersion on supported metal catalysts, Langmuir 13 (1997) 5613–5620.

[50] P. Yan, X. Tian, E.M. Kennedy, O.P. Tkachenko, M. Stockenhuber, Influence of promoters (fe, mo, W) on the structural and catalytic properties of Ni/BEA for guaiacol hydrodeoxygenation, ACS Sustainable Chem. Eng. 9 (2021) 15673–15682.

[51] J. Lin, C. Ma, Q. Wang, Y. Xu, G. Ma, J. Wang, H. Wang, C. Dong, C. Zhang, M. Ding, Enhanced low-temperature performance of CO₂ methanation over mesoporous Ni/Al₂O₃-ZrO₂ catalysts, Appl. Catal. b: Env. 243 (2019) 262–272.

[52] S. Ratchahat, M. Sudoh, Y. Suzuki, W. Kawasaki, R. Watanabe, C. Fukuhara, Development of a powerful CO₂ methanation process using a structured Ni/CeO₂ catalyst, J. CO2 Utilization 24 (2018) 210.

[53] E. Stavitski, M.H.F. Kox, B.M. Wecjhuysen, Revealing shape selectivity and catalytic activity trends within the pores of H-ZSM-5 crystals by time- and space-resolved optical and fluorescence microspectroscopy, chemistry a, European Journal 13 (2007) 7057–7065.

[54] P. Yan, M. Drewery, J. Mensah, J.C. Makie, E. Kennedy, M. Stockenhuber, Study on catalyst deactivation during the hydrodeoxygenation of model compounds, Top Catal. 63 (2020) 778–792.

[55] P. Yan, G. Bryant, M.M.J. Li, J. Mensah, E. Kennedy, M. Stockenhuber, Shape selectivity of zeolite catalysts for the hydrodeoxygenation of biocrude oil and its model compounds, Micro. Meso. Mater. 309 (2020) 110561–110574.

[56] J. Jae, G.A. Tompsett, A.J. Foster, K.D. Hammond, S.M. Auerbach, R.F. Lobo, G. W. Huber, Investigation into the shape selectivity of zeolite catalysts for biomass conversion, J. Catal. 279 (2011) 257–268.

[57] N. Mehio, S. Dai, D. Jiang, Quantum mechanical basis for kinetic diameters of small GaseousMolecules, J. Phy. Chem. A 118 (2014) 1150–1154.

[58] P. Yan, E. Kennedy, M. Stockenhuber, Natural zeolite supported ni catalysts for hydrodeoxygenation of anisole, Green Chem. 23 (2021) 4673–4684.

[59] J. van de Loosdrecht, A.M. ver der Kraan, A.J. van Dillen, J.W. Geus, Metal-support Interaction: titania-supported and silica-supported nickel catalysts, J. Catal. 170 (1997) 217–226.

[60] P. Yan, J. Mensah, A. Adesina, E. Kennedy, M. Stockenhuber, Highly-dispersed ni on BEA catalyst prepared by ion-exchange-deposition-precipitation for improved hydrodeoxygenation activity, Appl. Catal. b: Env. 267 (2020) 118690–118700.

[61] M. Che, Z. Cheng, C. Louis, Nucleation and Particle growth processes involved in the Preparation of silica-supported nickel materials by a two-step procedure, J. Am. Chem. Soc. 117 (1995) 2008–2018.

[62] M. Akri, S. Zhao, X. Li, K. Zang, A.F. Lee, M.A. Isaacs, W. Xi, Y. Gangarajula, J. Luo, Y. Ren, Y. Cui, L. Li, Y. Su, X. Pan, W. Wen, Y. Pan, K. Wilson, L. Li, B. Qiao, H. Ishii, Y. Liao, A. Wang, X. Wang, T. Zhao, Atomically dispersed nickel as coke-resistant active sites for methane dry reforming, Nature Commun. 10 (2019) 5181.

[63] Z. Hu, C. Wang, C. Chen, Z. Yuan, Catalytic decomposition of ammonia to COₓ-free hydrogen over Ni/ZSM-5 catalysts: a comparative study of the preparation methods, Appl. Catal. a: Gen. 562 (2018) 49–57.

[64] M.A. Peck, M.A. Langell, Comparison of nanoscaled and bulk NiO structural and environmental Characteristics by XRD, XAFS, and XPS, Chem. Mater. 24 (2012) 4483–4490.

LTA4A and zeolite LTA5A used as nickel catalyst supports for recycling carbon dioxide to green fuel methane, J. CO2 Utilization 55 (2022) 101803.

[65] E.L. Ratcliff, J. Meyer, K.X. Steirer, A. Garcia, J.J. Berry, D.S. Ginley, D.C. Olson, A. Kahn, N.R. Armstrong, Evidence for near-Surface NiOOH species in solution-processed NiO_x selective interlayer materials: impact on energetics and the performance of Polymer bulk heterojunction photovoltaics, Chem. Mater. 23 (2011) 4988–5000.

[66] T.S. Frantz, W.A. Ruiz, C.A. da Rosa, V.B. Mortola, Synthesis of ZSM-5 with high sodium content for CO_2 adsorption, Micro. Meso. Mater. 222 (2016) 209–217.

[67] J. Li, M. Gao, W. Yan, J. Yu, Regulation of the Si/Al ratios and al distributions of zeolites and their impact on properties, Chem. Sci. 14 (2023) 1935.

[68] M. Palomino, A. Corma, F. Rey, S. Valencia, New insights on CO_2−Methane Separation using LTA zeolites with different Si/Al ratios and a first Comparison with MOFs, Langmuir 26 (2010) 1910–1917.

[69] D. Beierlein, D. Haussermann, M. Pfeifer, T. Schwarz, K. Stowe, Y. Traa, E. Klemm, Is the CO_2 methanation on highly loaded ni-Al_2O_3 catalysts really structure-sensitive? Appl. Catal. b: Env. 247 (2019) 200–219.

[70] C. Liang, H. Tian, G. Guo, S. Zhang, Q. Liu, D. Dong, X. Hu, Methanation of CO_2 over alumina supported nickel or cobalt catalysts: effects of the coordination between metal and support on formation of the reaction intermediates, Int. J. Hydrogen Energy 45 (2020) 531–543.

[71] S. Sharma, K.B. Kumar, Y.M. Chandnani, V.S.P. Kumar, B.P. Gangwar, A. Singhal, P.A. Deshpande, Mechanistic insights into CO_2 methanation over ru-substituted CeO_2, J. Phy. Chem. C 120 (2016) 14101–14112.

[72] P. Yan, X. Tian, E.M. Kennedy, M. Stockenhuber, The role of ni sites located in mesopores in the selectivity of anisole hydrodeoxygenation, catal, Sci. Technol. 12 (2022) 2184–2196.

[73] B. Alrafei, I. Polaert, A. Ledoux, F. Azzolin-Jury, Remarkably stable and efficient ni and ni-co catalysts for CO_2 methanation, Catal. Today 346 (2020) 23–33.

[74] A. Vita, C. Italiano, L. Pino, P. Frontera, M. Ferraro, V. Antonucci, Activity and stability of powder and monolith-coated Ni/GDC catalysts for CO_2 methanation, Appl. Catal. b: Env. 226 (2018) 384–395.

[75] N. Garcia-Moncada, J.C. Navarro, J.A. Odriozola, L. Lefferts, J.A. Faria, Enhanced catalytic activity and stability of nanoshaped Ni/CeO_2 for CO_2 methanation in micro-monoliths, Catal. Today 383 (2022) 205–215.

[76] H. Muroyama, Y. Tsuda, T. Asaoshi, H. Masitah, T. Okanishi, T. Matsui, K. Eguchi, Carbon dioxide methanation over ni catalysts supported on various metal oxides, J. Catal. 343 (2016) 178–184.

[77] M.A.A. Aziz, A.A. Jalil, S. Triwahyono, M.W.A. Saad, CO_2 methanation over ni-promoted mesostructured silica nanoparticles: influence of ni loading and water vapor on activity and response surface methodology studies, Chem. Eng. J. 260 (2015) 757–764.

[78] M.S. Batista, E.I. Santiago, E.M. Assaf, E.A. Ticianelli, Evaluation of the water-gas shift and CO methanation processes for purification of reformate gases and the coupling to a PEM fuel cell system, J. Power. Sources 145 (2005) 50–54.

[79] J. Ren, F. Zeng, C. Mebrahtu, R. Palkovits, Understanding promotional effects of trace oxygen in CO_2 methanation over Ni/ZrO_2 catalysts, J. Catal. 405 (2022) 385–390.

[80] J. Ren, C. Mebrahtu, L. van Koppen, F. Martinovic, J.P. Hofmann, E.J.M. Hensen, R. Palkovits, Enhanced CO_2 methanation activity over $La_{2-x}Ce_xNiO_4$ perovskite-derived catalysts: understanding the structure-performance relationships, Chem. Eng. J. 426 (2021) 131760.